The Astrophysical Journal, 864:6 (15pp), 2018 September 1 https://doi.org/10.3847/1538-4357/aad37e

Active Galactic Nucleus Feedback in an Elliptical Galaxy with the Most Updated AGN Physics. II. High Angular Momentum Case

Doosoo Yoon[1], Feng Yuan[1,2], Zhao-Ming Gan[1], Jeremiah P. Ostriker[3], Ya-Ping Li[1], and Luca Ciotti[4]
[1] Key Laboratory for Research in Galaxies and Cosmology, Shanghai Astronomical Observatory, Chinese Academy of Sciences, 80 Nandan Road, Shanghai 200030, People's Republic of China; yoon@shao.ac.cn
[2] University of Chinese Academy of Sciences, 19A Yuquan Road, 100049, Beijing, People's Republic of China; fyuan@shao.ac.cn
[3] Department of Astronomy, Columbia University, 550 W. 120th Street, New York, NY 10027, USA
[4] Department of Physics and Astronomy, University of Bologna, via Piero Gobetti 93/2, I-40129 Bologna, Italy
Received 2018 March 9; revised 2018 July 2; accepted 2018 July 11; published 2018 August 24

Abstract

This is the second paper of our series of works of studying the effects of active galactic nuclei (AGNs) feedback on the cosmological evolution of an isolated elliptical galaxy by performing two-dimensional hydrodynamical simulations. Compared to previous works, the main improvement here is that we adopt the most up-to-date AGN physics, which is described in detail in the first paper, including the discrimination of the two accretion modes and the most up-to-date descriptions of the wind and radiation in the two modes. In Paper I, we consider the case that the specific angular momentum of the gas in the galaxy is very low. In this paper, we consider the case that the specific angular momentum of the gas is high. At the galactic scale, we adopt the gravitational torques raised due to non-axisymmetric structure in the galaxy as the mechanism of the transfer of angular momentum of gas, as proposed in some recent works. Because our simulations are axisymmetric, we make use of a parameterized prescription to mimic this mechanism. Special attention is paid to the effects of specific angular momentum of the galaxy on the AGN light curve, growth of the black hole mass, AGN duty-cycle, star formation, and the X-ray surface brightness. We find that some results are qualitatively similar to those shown in Paper I, while other results, such as star formation and black hole growth, show a significant difference due to the mass concentration in the galactic disk as a consequence of galactic rotation.

Key words: accretion, accretion disks – black hole physics – galaxies: active – galaxies: elliptical and lenticular, cD – galaxies: evolution – galaxies: nuclei

1. Introduction

It is now believed that most massive galaxies harbor supermassive black holes in their central regions, and these black holes play a crucial role in the evolution of their host galaxies. The underlying mechanism is known as active galactic nucleus (AGN) feedback, which implies that changes to the density and temperature of the interstellar medium (ISM) in the galaxy are due to the radiation and outflow from the AGN, as are subsequent changes in star formation and black hole fueling (Fabian 2012; Kormendy & Ho 2013, and references therein).

To evaluate the effects of AGN feedback on galaxy evolution by numerical simulations, we ideally ought to simulate from the central black hole to the whole galaxy, i.e., from the BH Schwarzschild radius of $R_s \sim 10^{-5}\,\mathrm{pc}\,(M_{\rm BH}/10^8\,M_\odot)$ to the galaxy scale of ∼100s kpc. However, the ratio of the size scale of the black hole to that of the host galaxy is more than ten orders of magnitude, so it is not feasible to cover such a large dynamical range even with a state-of-art supercomputer. Therefore, different works in the literature focus on different spatial scales. Most of the works focus on a scale much larger than the black hole accretion flow. In this case, the AGN is difficult to resolve, and a so-called "sub-grid" model to describe the AGN physics has been developed and widely used in many simulations.

In this case, it obviously is crucial to have a correct description of the output from the central AGN. Then the first important parameter is the mass accretion rate of the AGN. Many works focus on such large scales that it is difficult to resolve the Bondi radius and calculate the accretion rate directly. In those cases, the accretion rates have to be estimated in some way; ergo, the value can be significantly underestimated or overestimated (e.g., Negri & Volonteri 2017 and references therein; see also Korol et al. 2016; Ciotti & Pellegrini 2017) Some other works, which focus on relatively smaller scales, overcome this problem by resolving the Bondi radius (Ciotti & Ostriker 1997, 2001, 2007; Ciotti et al. 2009b, 2017; Ostriker et al. 2010; Shin et al. 2010; Novak et al. 2011, 2012; Gan et al. 2014). In these works, the inner boundary is set to be a few pc, which is smaller than the Bondi radius, so we can directly calculate (rather than estimate) the mass accretion rate at the inner boundary. The outer boundary is large enough to reach ∼100s of kpc, allowing the study of the evolution of the whole galaxy and even the circumgalactic medium (CGM).

Once the mass accretion rate is reliably calculated, the output of the AGN, namely the radiation and wind (jet is neglected in our work), is determined by the accretion physics adopted (e.g., see the review of accretion theory by Yuan & Narayan 2014). Most recently, by taking into account the recent developments of the theory of black hole accretion, Yuan et al. (2018, hereafter Paper I) have presented the most up-to-date descriptions of the AGN outputs. In this work, we have investigated the AGN feedback effects in an isolated elliptical galaxy by performing two-dimensional hydrodynamical numerical simulations. The inner boundary of the simulation is chosen such that the Bondi radius is resolved and the accretion rate is precisely determined. We discriminate between the cold and hot accretion modes according to the value of the accretion rate, and present proper descriptions of wind and radiation emitted from the accretion flow in the two modes. Our numerical results indicate that these updates of the

AGN physics are crucial for determining the effects of AGN feedback. The updated AGN physics is described in detail in Paper I, but will be briefly reviewed in Section 3 of the present paper.

In Paper I, the specific angular momentum of the gas in the galaxy is assumed to be very small. Although elliptical galaxies are primarily pressure-supported rather than rotation-supported, the angular momentum of the gas in many galaxies is likely not small. Recent kinematic surveys have revealed that ∼80% of early-type galaxies (ETGs) belong to regular rotators, characterized by oblate axisymmetric shapes that reflect underlying disk-like components (Emsellem et al. 2011; Krajnović et al. 2011, 2013). Even in the slowly rotating ETGs, a midplane HI disk, indicative of the presence of a stellar disk, is frequently detected (Serra et al. 2014).

The goal of this work is to extend Paper I by considering the case of higher angular momentum. In this study (but not in Paper I), we study the physical mechanism of angular momentum transport. As we will describe later, it seems as if different mechanisms play their respective roles on different scales. On the galactic scale, one of the most promising mechanisms is the gravitational torque raised by the non-axisymmetric structure of stars in the galaxy, as proposed in Hopkins & Quataert (2010, 2011). As our simulation is two-dimensional, it is impossible to include such a mechanism from first principles. Instead, we adopt a phenomenological approach by using the α-description, similar to the case of black hole accretion disk (Shakura & Sunyaev 1973). This α-description was devised with a physically motivated, dimensionless scaling of the kinematic viscosity such that the strength of the angular momentum transport process would be represented in dimensionless fashion by α. The detailed implemention in our work is presented in Section 4.1.

In the present work, we ignore AGN activity triggered by an external mechanism, such as galactic mergers. Although the mergers may be effective in triggering AGN activity (Mihos & Hernquist 1996; Di Matteo et al. 2005), there are reasons that the assumption of an isolated galaxy is worth considering. First, observations indicate that BH growth in massive galaxies is likely driven by internal secular processes rather than by significant mergers, at least since redshift $z \sim 2$ (Schawinski et al. 2011; Kocevski et al. 2012; Fan et al. 2014). Second, even in the absence of merging, the total amount of gas injected from the pure stellar evolution is large enough to produce a BH two orders of magnitudes more massive than what is observed (Ciotti & Ostriker 2012). In the future, we will examine the effect of galactic merging on the evolution of the central black hole and its host galaxy. It is speculated that the gas contents may be enhanced, which may then induce both star formation and AGN activity, especially in early evolution time.

As the second paper of a series of project, in this work we extend the work of Paper I to the case of an elliptical galaxy that is partly rotation-supported rather than fully pressure-supported. The paper is organized as follows. In Section 2, we describe the detailed model of the galaxy. In Section 3, we briefly review the updated AGN physics that we adopt in the simulation. In Section 4, we present the numerical setup and treatment of angular momentum transport. In Section 5, we describe the simulation results, including the AGN light curve, growth of black hole mass, star formation, and X-ray emission of the galaxy. A summary and our conclusions are presented in Section 6.

2. Galaxy Models

In this section, we briefly introduce the key features of the galaxy models, with respect to the stellar population and evolution, the dynamical structure, and the galaxy's rotation. To isolate the problem, we set the many aspects of the simulations to be same as those in Gan et al. (2014) (see also Novak et al. (2011) for more detailed description), except for the treatment of galactic rotation (see Section 2.2).

2.1. Stellar Evolution

In elliptical galaxies, the gas is supplied by evolved stars predominantly in the phases of the red giant, asymptotic giant branch, and planetary nebula. The total mass of gas injected from the pure passive stellar evolution is two orders of magnitudes larger than the BH mass observed in elliptical galaxies (Ciotti & Ostriker 2012). In our simulation, the gas density is initially set to be low so that the gas is mainly supplied from stellar evolution, i.e., "secular evolution."

Following the description in Pellegrini (2012), the total mass-loss rate of a stellar population is computed by

$$\dot{M}(t) = \dot{M}_{\star}(t) + \dot{M}_{\rm SN}(t), \tag{1}$$

where $\dot{M}_{\star}$ is the mass-loss rate for an evolved star, which is approximated as the single-burst stellar population synthesis model (Maraston 2005),

$$\dot{M}_{\star} = 10^{-12}\, A \times M_{\star}\, t_{12}^{-1.3} \quad M_{\odot}\ {\rm yr}^{-1}, \tag{2}$$

where $M_{\star}$ is the galactic stellar mass in solar mass units at an age of 12 Gyr, and t_{12} is the age in units of 12 Gyr. For all models, we set the galactic stellar mass to $M_{\star} = 3 \times 10^{11}\, M_{\odot}$ and the coefficient A is set to be 3.3, which is indicative of Kroupa initial mass function. The recycled rate of gas from SNIa is $\dot{M}_{\rm SN} = 1.4\, M_{\odot}\, R_{\rm SN}(t)$, where $R_{\rm SN}$ is the evolution of the explosion rate with time. The approximate mass-loss rate, Equation (1), is reliable for solar metal abundance.

2.2. Galactic Structure

The galaxy models are built following the procedure described elsewhere (Ciotti et al. 2009a), and refer to an isolated elliptical galaxy placed on the fundamental plane with a projected stellar velocity dispersion, considering a spherically symmetric dark matter halo and stellar profile. The stellar density profile is described by the Jaffe profile (Jaffe 1983),

$$\rho_{\star} = \frac{M_{\star}\, r_{\star}}{4\pi r^2 (r_{\star} + r)^2}, \tag{3}$$

where $M_{\star}$ and $r_{\star}$ are the total stellar mass and the scale length of the galaxy, respectively. In this paper, we set the total stellar mass to $M_{\star} = 3 \times 10^{11}\, M_{\odot}$ and the scale length to $r_{\star} = 9.2$ kpc, which corresponds to the projected half-mass radius (i.e., effective radius) of $r_e = 0.7447\, r_{\star} = 6.9$ kpc. The dark halo profile is set by the total density profile scaling as $\rho \propto r^{-2}$ at large radii, which is consistent with observed profiles (Czoske et al. 2008; Dye et al. 2008; Auger et al. 2010; Sonnenfeld et al. 2013).

We adopt the central velocity dispersion of $\sigma_0 = 260\,{\rm km\,s^{-1}}$. For the minimum halo model, the systematic rotational velocity,

Table 1
Description of the Simulations

Model	k	$\alpha_{\rm visc}$	Mechanical Feedback	Radiative Feedback
k00[a]	0	0.1	o	o
k01	0.1	0.1	o	o
k03	0.3	0.1	o	o
k05[b]	0.5	0.1	o	o
k07	0.7	0.1	o	o
k09	0.9	0.1	o	o
k05noFB	0.5	0.1	x	x
k05windFB	0.5	0.1	o	x
k05radFB	0.5	0.1	x	o
k05alp-2	0.5	0.01	o	o

Notes.
[a] k00 is the same model as fullFB in Paper I.
[b] Fiducial model in this paper.

v_c of the galaxy is computed as

$$v_c = \sqrt{2}\,\sigma_0 = 368\ {\rm km\ s^{-1}}. \quad (4)$$

In this model, the gas flows under the total gravitational potential of

$$\Phi_{\rm tot} = v_c^2\,\ln\left(\frac{r}{r_\star}\right). \quad (5)$$

As discussed in Section 2.1, most of gas is supplied by stellar evolution. Therefore, the angular momentum of the gas, which is ejected through the stellar wind (i.e., mass losses from asymptotic giant branch stars), is initially set by the rotating motion of stellar components. We introduce the rotation factor, k, to set the degree of the stellar rotation, which is described as

$$v_{\phi,\star} = k\,\sin\theta\,\sigma_r, \quad (6)$$

where σ_r is the isotropic one-dimensional stellar velocity dispersion without the contribution of the central black hole:

$$\sigma_r^2 = \sigma_0^2(1+s)^2 s^2\left[6\ln\left(\frac{1+s}{s}\right) + \frac{1-3s-6s^2}{s^2(1+s)}\right], \quad (7)$$

where $s \equiv r/r_\star$. We perform the subsets of simulations with $k = 0.1, 0.3, 0.5, 0.7, 0.9$ (see Table 1), and thus the supplied gas from the stellar evolution rotates with sub-Keplerian velocity. However, as it falls into the midplane disk, the angular momentum of the infalling gas reaches the Keplerian value (see Figure 8).

From the perspective of energetics, the thermalization of the stellar mass losses due to the stellar velocity dispersion should be taken into account (Parriott & Bregman 2008). The amount of the thermalization heating decreases as the stellar rotation velocity increases, because the ordered motion becomes dominant compared to the random motion of the stars. A detailed description of the thermalization is provided in Section 4.1.

A central black hole also contributes to the gravitational potential, with its dominance limited to the central region. The initial BH mass is chosen by the empirical correlation between the black hole mass and the bulge mass in (Kormendy & Ho 2013), which is

$$M_{\rm BH} = 5\times10^8\,M_\odot\left(\frac{M_\star}{10^{11}\,M_\odot}\right)^{1.17}. \quad (8)$$

Given our fiducial galactic stellar mass, the initial black hole mass is set to $M_{\rm BH,init} = 1.8\times10^9\,M_\odot$ for all models.[5]

Various shapes and internal kinematics of galaxy models were taken into account in a previous study of X-ray halos in ETGs by Negri et al. (2014). In that work, they adopted axisymmetric galaxy models for which the galaxies are flattened by either non-isotropic stellar velocity dispersion or rotation. However, they ignored the effects of AGN feedback, which likely plays a significant role in producing X-ray radiation in the central region (see Paper I). In a following work, Ciotti et al. (2017) applied this axisymmetric galaxy model to the numerical study of AGN feedback. In that work, the flattening was set to occur by the non-isotropic stellar velocity dispersion without consideration of the galactic rotation. Although our galaxy model is spherically symmetric to isolate the problem in Paper I, in the present work, we consider both galactic rotation and AGN feedback to understand their respective roles in the evolution of the black hole and its host galaxy. In the following study, axisymmetric galaxy models will be also taken into account.

2.3. Angular Momentum Transport

The inflow of gas into the galactic center is essential to manipulate active star formation and switch on the AGN activity. The triggers of such inflows are diverse, and the dominant one depends on the scale: on a galactic scale, tidal torques driven by major mergers or cosmological infall lead to rapid gas inflow into the central ∼kpc (Hernquist 1989; Barnes & Hernquist 1991, 1996). Minor mergers and/or disk instabilities, which cause bar and spiral structures, may also produce similar gravitational torques (Hernquist & Mihos 1995; Bournaud et al. 2005; Younger et al. 2008). Once gas reaches sub-kpc scales, it cools rapidly, which can cause a non-axisymmetric gravitational instability and torque, and thus a large fraction of the gas can flow toward the central region at ∼0.01 pc (Bertin & Lodato 2001; Lodato & Rice 2004; Hopkins & Quataert 2010, 2011). Near the central BH, it is believed that MHD turbulence, produced by magnetorotational instability, is responsible for the angular momentum transport (Balbus & Hawley 1991, 1998).

In our simulation, we consider the secular evolution of elliptical galaxies without merger events. As we will discuss, for most of our simulation, as the gas cools down, it forms a midplane disk at the scale of ∼kpc, within which the gravitational torques by non-secondary instabilities are favored to be the dominant mechanism for the angular momentum transport (Hopkins & Quataert 2010, 2011). However, because we perform the simulations in two dimensions without considering self-gravity of the gas, we technically cannot include the non-axisymmetric torque. As an alternative approach, we make use of stress tensor, $\boldsymbol{T}$, with the viscosity α-prescription (Shakura & Sunyaev 1973) to mimic the gravitational disturbances exerting on the gas. (see Section 4.1 for the detailed description). While the proper $\alpha_{\rm visc}$ value is largely uncertain, we set it to the fiducial

[5] We note here that there is some uncertainty in this value and Equation (12) of Kormendy & Ho (2013): for our chosen value of $\sigma_0 = 260\ {\rm km\ s^{-1}}$, the corresponding black hole mass is $M_{\rm BH} = 9\times10^8\,M_\odot$.

value of $\alpha_{\rm visc} = 0.1$ for most runs. For this value of α, in our fiducial model, k05, the gas inflow at ~100s pc from the disk is $0.1 \sim 10\,M_\odot\ {\rm yr}^{-1}$. This value is roughly consistent with the median value of the inflow rate obtained in Hopkins & Quataert (2011), although the latter has larger scatter.

Hopkins & Quataert (2010) showed that a gas-rich galaxy merger can induce the gas inflow rate up to $100\,M_\odot\ {\rm yr}^{-1}$ at 300 pc. Compared to the case of gas-rich galaxy merger, it is not surprising that gas inflow rate in our results is small because we focus on the "secular" evolution of galaxy, which is initially gas-poor. Even for the model without galactic rotation, the model k00, the large-scale inflow is a few $10\,{\rm s}\,M_\odot\ {\rm yr}^{-1}$, which is larger than in the model k05, but still smaller than in the case of gas-rich merger, mainly due to the dearth of initial gas in our galactic model. However, as we will discuss, the gas inflow rate in the present work is large enough to trigger a luminous AGN.

3. Physical Model of AGN Feedback

We adopt the most up-to-date "sub-grid" AGN physics presented in Paper I. For completeness, we briefly review it as follows.

The first important thing to note is that, depending on the value of the accretion rate, black hole accretion is divided into two modes. When the accretion rate is relatively high, it belongs to the cold accretion mode. The most luminous AGN, such as quasars, are in this mode. When the accretion rate is lower, it shifts to the hot accretion mode, in which AGNs spend most of their time. The two modes are bounded by a critical luminosity,

$$L_{\rm c} \approx 2\%\ L_{\rm Edd}. \tag{9}$$

The cold and hot accretion modes are described by the standard thin disk (Shakura & Sunyaev 1973) and the hot accretion flows, respectively (Yuan & Narayan 2014). These are two completely different accretion modes in the sense of the dynamics and radiation of the accretion flows. For the cold mode, many mechanisms seem to play a role in producing wind, such as thermal, magnetic, and radiation (line-force) (see Proga 2003), and theoretically the wind production is still a partially solved problem. Therefore, we adopt the observational results of Gofford et al. (2015) to describe the wind properties. The mass, momentum, and energy fluxes of the winds are described by

$$\dot{M}_{\rm W,C} = 0.28\left(\frac{L_{\rm bol}}{10^{45}\ {\rm erg\ s^{-1}}}\right)^{0.85} M_\odot\ {\rm yr}^{-1}, \tag{10}$$

$$\dot{P}_{\rm W,C} = \dot{M}_{\rm W,C}\, v_{\rm W,C}, \tag{11}$$

$$\dot{E}_{\rm W,C} = \frac{1}{2}\dot{P}_{\rm W,C}\, v_{\rm W,C}, \tag{12}$$

where $L_{\rm bol}$ is the bolometric luminosity of the AGN. The velocity of wind is described by

$$v_{\rm W,C} = 2.5 \times 10^4 \left(\frac{L_{\rm bol}}{10^{45}\ {\rm erg\ s^{-1}}}\right)^{0.4} {\rm km\ s^{-1}}, \tag{13}$$

and we set the maximum wind velocity of $10^5\,{\rm km\,s^{-1}}$.

The radiation from the thin disk is well-known: it is approximated as

$$L_{\rm bol} = \epsilon_{\rm EM,cold}\,\dot{M}_{\rm BH} c^2, \tag{14}$$

where $\dot{M}_{\rm BH}$ is the BH accretion rate, c is the speed of light, and $\epsilon_{\rm EM,cold}$ is the radiative efficiency. Here, we assume the value of the efficiency in cold mode is 0.1, implying that the BH is moderately spinning. This value also agrees with the empirical studies of Yu & Tremaine (2002) and Soltan (1982). In addition to luminosity, another important parameter to describe the radiative heating to the ISM of the host galaxy by Compton scattering is the Compton temperature of the radiation. In the cold mode, its value is $T_{\rm C} \approx 10^7$ K (Sazonov et al. 2004).

The black hole mass accretion rate in the cold mode is calculated by

$$\dot{M}_{\rm BH,cold} = \dot{M}_{\rm d,inflow} - \dot{M}_{\rm W,C}, \tag{15}$$

where $\dot{M}_{\rm d,inflow}$ is the mass inflow rate in the accretion disk around the black hole with the instantaneous viscous timescale, $\tau_{\rm visc} \approx 10^6$ years (see Paper I for more detailed description).

In the hot accretion mode, the geometry of the accretion flow is usually an inner hot accretion flow plus an outer truncated thin disk (Yuan & Narayan 2014). The truncation radius is described by

$$R_{\rm tr} \approx 3\,R_s\left[\frac{2\times 10^{-2}\,\dot{M}_{\rm Edd}}{\dot{M}(r_{\rm Bondi})}\right]^2, \tag{16}$$

where R_s is the Schwarzschild radius, which is $R_s \equiv 2\,G\,M_{\rm BH}/c^2$. In contrast to the case of the cold accretion mode, wind production in the hot mode is theoretically well-studied (e.g., Yuan et al. 2012, 2015; Bu et al. 2016), but the observational constraints are much worse due to the lack of observational data. Using the trajectory approach, Yuan et al. (2015) have carefully calculated the fluxes of mass, momentum, and energy of wind based on the GRMHD simulation of black hole accretion:

$$\dot{M}_{\rm W,H} \approx \dot{M}_{r_{\rm Bondi}}\left[1 - \left(\frac{3\,r_s}{r_{\rm tr}}\right)^{0.5}\right], \tag{17}$$

$$\dot{P}_{\rm W,H} = \dot{M}_{\rm W,H}\, v_{\rm W,H}, \tag{18}$$

$$\dot{E}_{\rm W,H} = \frac{1}{2}\dot{M}_{\rm W,H}\, v_{\rm W,H}^2, \tag{19}$$

where $r_{\rm Bondi}$ is the Bondi radius and the wind velocity is approximated as

$$v_{\rm W,H} \approx (0.2 - 0.4)\, v_{\rm K}(r_{\rm tr}), \tag{20}$$

where $v_{\rm K}$ is the Keplerian velocity.

The black hole accretion rate in the hot mode is computed by

$$\dot{M}_{\rm BH,hot} \approx \dot{M}_{r_{\rm Bondi}}\left(\frac{3\,r_s}{r_{\rm tr}}\right)^{0.5}. \tag{21}$$

Because hot accretion flows are optically thin, the radiation output from hot accretion flows is much more complicated than that from the cold mode (Yuan & Narayan 2014). In this case, the radiative efficiency is no longer a constant. The radiative efficiency as a function of accretion rate is studied in Xie &

Yuan (2012), which gives the following fitting formula:

$$\epsilon_{\rm EM,hot}(\dot{M}_{\rm BH}) = \epsilon_0 \left(\frac{\dot{M}_{\rm BH}}{0.1\, L_{\rm Edd}/c^2} \right)^a, \quad (22)$$

where the value of ϵ_0 and a are given in Xie & Yuan (2012). Here, we summarize the set of (ϵ_0, a) that is adopted for the current work.

$$(\epsilon_0,\, a) = \begin{cases} (0.2,\, 0.59), & \dot{M}_{\rm BH}/\dot{M}_{\rm Edd} \lesssim 9.4 \times 10^{-5} \\ (0.045,\, 0.27), & 9.4 \times 10^{-5} \lesssim \dot{M}_{\rm BH}/\dot{M}_{\rm Edd} \lesssim 5 \times 10^{-3} \\ (0.88,\, 4.53), & 5 \times 10^{-3} \lesssim \dot{M}_{\rm BH}/\dot{M}_{\rm Edd} \lesssim 6.6 \times 10^{-3} \\ (0.1,\, 0), & 6.6 \times 10^{-3} \lesssim \dot{M}_{\rm BH}/\dot{M}_{\rm Edd} \lesssim 2 \times 10^{-2}. \end{cases} \quad (23)$$

The Compton temperature is higher than that of the cold mode, due to the difference of the emitted spectrum between cold and hot modes. Its values are $T_c \approx 10^8$ K and 5×10^7 K for the ranges of $10^{-3} \lesssim L/L_{\rm Edd} \lesssim 0.02$ and $L/L_{\rm Edd} \lesssim 10^{-3}$, respectively (Xie et al. 2017).

4. Numerical Setup

We perform two-dimensional hydrodynamic simulations with ZEUS-MP2 (Hayes et al. 2006) in spherical coordinates (r, θ). The grid resolution is 120×30. The grid bin size in the radial direction increases logarithmically and the range covers 2.5 pc $\sim$ 250 kpc. A simulation with such a large dynamical range is computationally expensive, hence we choose the two-dimensional simulation assuming the axisymmetry. However, this approximation has difficulty in resolving instabilities and non-axisymmetric features such as spiral structures. In following work, we will extend this work to three dimensions. We note that the Bondi radius is determined by the physical properties at the galactic center: $r_{\rm Bondi} = G\, M_{\rm BH}/c^2_{s,\rm in} \approx 10\ {\rm pc}\, (M_{\rm BH}/3 \times 10^8\, M_\odot)\, (T/10^7\ {\rm K})^{-1}$ (Bondi 1952), where $c_{s,\rm in}$ is the sound speed of the gas at the inner boundary. The Bondi radius varies during simulations, but most of the time it is well-resolved, which enables us to estimate the proper BH accretion rate.

Galaxy mergers may be responsible for inducing star formation in the central region, as well as fueling the BH and thus providing the power source of the quasar state at early cosmic times (e.g., Mihos & Hernquist 1996; Di Matteo et al. 2005; Cortijo-Ferrero et al. 2017). The rapid growth of the BH and the possible formation of elliptical galaxies via merging process is beyond the scope of the current paper. However, observations indicate that the hosts of AGNs are likely to evolve secularly rather than being involved in an ongoing merger since $z \sim 2$ (Schawinski et al. 2011; Kocevski et al. 2012; Fan et al. 2014). In our simulation, we assume that the galaxy is initially well-established and evolves secularly. The simulations begin at a galaxy age of $\sim$2 Gyr, which corresponds to the redshift $z \sim 3$; for the comprehensive study, the evolution time spans 14 Gyr.

4.1. Hydrodynamics

The evolution of the galactic gas flow is computed by integrating the time-dependent Eulerian equations for conservation of mass, momentum, and energy:

$$\frac{\partial \rho}{\partial t} + \nabla \cdot (\rho \boldsymbol{v}) = \alpha_\star \rho_\star + \dot{\rho}_{\rm II} - \dot{\rho}^+_\star, \quad (24)$$

$$\frac{\partial \boldsymbol{m}}{\partial t} + \nabla \cdot (\boldsymbol{m}\boldsymbol{v}) = -\nabla p_{\rm gas} + \rho \boldsymbol{g} - \nabla p_{\rm rad} - \dot{\boldsymbol{m}}^+_\star + \nabla \cdot \boldsymbol{T}, \quad (25)$$

$$\frac{\partial E}{\partial t} + \nabla \cdot (E\boldsymbol{v}) = -p_{\rm gas} \nabla \cdot \boldsymbol{v} + H - C + \dot{E}_I + \dot{E}_{\rm II} + \dot{E}_S - \dot{E}^+_\star + \boldsymbol{T}^2/\mu, \quad (26)$$

where ρ, $\boldsymbol{m}$, and E are the gas mass, momentum, and internal energy per unit volume, respectively. The gas pressure is $p_{\rm gas} = (\gamma - 1)\, E$, where the specific heats is $\gamma = 5/3$. Here, $\alpha_\star \rho_\star$ is the mass source from the stellar evolution, and $\dot{\rho}_{\rm II}$ is the recycled gas from supernovae (SNe) II. We let the source term $\alpha_\star \rho_\star$ evolve passively with Salpeter initial mass function (Salpeter 1955). In these equations, $\dot{E}_I$ and $\dot{E}_{\rm II}$ are feedback from SNe I and SNe II, respectively: $\dot{E}_I = \dot{\rho}_{\rm Ia}\, \vartheta_{\rm SNIa}\, E_{\rm SN}/(1.4\, M_\odot)$, where the kinetic energy of a single SNIa is $E_{\rm SN} = 10^{51}$ erg and the thermalization efficiency $\vartheta_{\rm SNIa} = 0.85$, which is reliable to low density and hot medium, where most SNe I occur (see Mathews 1989; Tang & Wang 2005). When gas turns into stars, we eliminate the corresponding mass, momentum, and energy ($\dot{\rho}^+_\star$, $\dot{\boldsymbol{m}}^+_\star$, $\dot{E}^+_\star$) to conserve quantities, but also add new mass and energy from SNII explosions ($\dot{\rho}_{\rm II}$, $\dot{E}_{\rm II}$). Under the assumption of a Salpeter initial mass function, the mass and the energy returned in SNII events for each star formation episode is 20% of the newly born star and their ejection timescale is $\tau_{\rm II} = 2 \times 10^7$ years. All parameters in the description of the stellar feedback are same for every model; see Negri et al. (2015) and Ciotti et al. (2017) for more detailed descriptions of stellar feedback.

In the energetics of the gas flows, the thermalization of the stellar mass loss, interacting with the preexisting hot ISM due to the stellar velocity dispersion, is important. In our galactic model, the stars have a certain degree of the ordered motion, so the thermalization heating, $\dot{E}_S$, is computed by the trace of the velocity dispersion, which is expressed as

$$\dot{E}_S = \frac{\alpha_\star \rho_\star}{2} \left[{\rm Tr}(\sigma^2) - v^2_{\phi,\star} \right] = \frac{\alpha_\star \rho_\star}{2} \left(1 - \frac{\sin^2\theta\, k^2}{3} \right) {\rm Tr}(\sigma^2), \quad (27)$$

in which the reduction factor $1 - \sin^2\theta\, k^2/3$ takes the effect of ordered rotation into account.

In Equation (25), we assume that the divergence of the tensor is strongest at the azimuthal components, which can be approximated as

$$\nabla \cdot \boldsymbol{T} \approx \left(\frac{\partial T_{r\phi}}{\partial r} + \frac{1}{r} \frac{\partial T_{\theta\phi}}{\partial \theta} + \frac{3\, T_{r\phi} + 2 \cot\theta\, T_{\theta\phi}}{r} \right) \hat{\phi}, \quad (28)$$

where, in spherical coordinates, the stress components are

$$\boldsymbol{T}_{r\phi} \approx \mu\, r \frac{\partial}{\partial r} \left(\frac{v_\phi}{r} \right), \quad (29)$$

$$\boldsymbol{T}_{\theta\phi} \approx \frac{\mu \sin\theta}{r} \frac{\partial}{\partial \theta} \left(\frac{v_\phi}{\sin\theta} \right). \quad (30)$$

Here, $\mu \equiv \rho\nu$ is the coefficient of shear viscosity, where ν is the kinematic viscosity coefficient,

$$\nu = \alpha_{\rm visc}\frac{c_s^2}{\Omega_{\rm k}}, \quad (31)$$

where c_s is the sound speed, $\Omega_{\rm k}$ is the Keplerian angular velocity, and $\alpha_{\rm visc}$ is the viscosity parameter formulated by Shakura & Sunyaev (1973). Note that, in this work, the simulation is performed with axisymmetric two-dimensional coordinates, so we neglect the derivative terms of ϕ directions and approximate the tensors to Equations (29) and (30). The numerical treatment of angular momentum transport by an anomalous tensor is done as in Stone et al. (1999). We adopt the value $\alpha_{\rm visc} = 0.1$ as a fiducial model; for comparison, we also perform a subset of test simulations with a value of $\alpha_{\rm visc}$ that is smaller by an order of magnitude (see Section 5.2).

5. Results

In this work, we allow for the possibility of gas with high angular momentum being deposited by the rotating stars. The rotation speed of stars is determined by the parameter k, which varies from 0 (k00; no rotation) to 0.9. Like Paper I, we also carry out a subset of simulations to compare the results from one with both radiative feedback and mechanical feedback (k00, k01, k03, k05, k07, k09), one with purely radiative feedback (k05radFB), one with purely mechanical feedback (k05windFB), and one without AGN feedback (k05noFB). Note that, for the models with no/partial feedback, the rest configurations are same as k05. All these models are listed in Table 1.

5.1. Overview of the Evolution

In Paper I, where the specific angular momentum of the gas in the galaxy is assumed to be very small, the overall evolution of the AGN is as follows. In the early stage, the gas is enriched by stellar mass loss, and when it reaches sufficient density, the ISM undergoes radiative cooling and produces cold shells and filamentary structures. These structures are unstable due to the Rayleigh–Taylor instability, then become disrupted in a short time. The disrupted gas flows inward toward the center and triggers the AGN activity. The strong radiation and winds produced by the AGN heat the medium and expel the gas out of the central region, thus suppressing the black hole accretion. The AGN activity is then reduced. As the ISM is replenished by stellar winds and gradually cools down, the AGN cycle will start over. This is the evolutionary track of the AGN cycle, which was inferred by the numerical results with the slowly rotating (or non-rotating) galaxy models in the previous studies.

In the present paper, we focus on a case where the gas in the galaxy has much higher angular momentum. While the general evolution picture of AGN activity is qualitatively similar, the details are significantly different. Figure 1 shows the overview of an AGN cycle in the rotating galaxy. From left to right, it shows the density map and gas streams in preburst, ongoing-burst, postburst, and quiescent periods, respectively. While the gas with low angular momentum accretes onto the BH from random directions, the gas with high angular momentum collapses into the midplane and flows toward the center along the disk (leftmost panel). Because the density of the disk is high, on the path toward the BH, the gas is largely consumed by the active star formation in the disk. The relative predominance between the BH accretion rate versus the star formation rate will be discussed in Section 5.4.

The gas in the disk likely loses its angular momentum via various physical mechanisms, such as magnetorotational instability (Stone & Pringle 2001), thermal instability (Bertin & Lodato 2001), gravitational instability (Toomre 1964; Gammie 2001), and non-axisymmetric gravitational torque (Hopkins & Quataert 2010, 2011; Anglés-Alcázar et al. 2017). It is believed that no single mechanism is dominant over a range of a few kpc from the BH event horizon, and their relative importance depends on the scale of interest (see Dorodnitsyn et al. 2016 and references therein). As the gas loses its angular momentum and accretes onto the central BH, the AGN activity is triggered (second panel). Similar to the case of the nonrotating model, the AGN feedback influences the surrounding medium via both the radiation and the mechanical winds. The radiation heats the central region, within which the cold disk is likely photoionized and heated. The AGN winds blowing out at a certain inclination angle are capable of generating turbulence, which disturbs the cold disk inside-out (third panel). Recently, Tacchella et al. (2015) found evidence that the star formation in the galactic disk is suppressed from the inside out. Our numerical results indicate that the energy released from the central AGN drives such inside-out star formation features. Finally, stellar mass loss replenishes the galaxy, the gas falls to the midplane again (rightmost panel), and a new AGN cycle begins. We note that the key difference between the AGN cycles of the slowly and rapidly rotating galaxies is the presence of the midplane disk, which alters the gas fueling channel to the central black hole. Many elliptical galaxies are indeed observed to contain central disks (e.g., Serra et al. 2014).

5.2. Light Curve of AGN Luminosity

Figure 2 shows the evolution of light curves of AGN luminosity. Here, k00 represents the model without galactic rotation, while k01, k05, and k09 represent the models in which the degree of the angular momentum increases in order.

The overall shapes of the light curves are similar for every model with the full AGN feedback, indicating that the effects of rotation on the galactic evolution may not be significant. However, there are several aspects that reveal trends as the level of angular momentum is varied. It is notable that, as the galaxy rotates slower, the AGN burst occurs more frequently at early evolution times and the peak of the burst tends to be higher. This is because the lower angular momentum provides a weaker barrier to hamper the BH accretion, producing the stronger AGN burst.

Most of the time, the AGN stays in the hot mode (i.e., the low-accretion regime; $L_{\rm BH} < 0.02\,L_{\rm Edd}$) as is observed. In the left panel of Figure 2, the horizontal dashed lines represent the mean value of the light curves in the hot mode. We found that the mean value increases gradually as the host galaxy rotates faster. In the most rapidly rotating model, k09, the mean value is a factor of six larger than in the non-rotating model, k00. This is because, in the case of lower angular momentum, the AGN activity can reach a higher level due to the easier accretion of the gas. Consequently, the AGN can produce

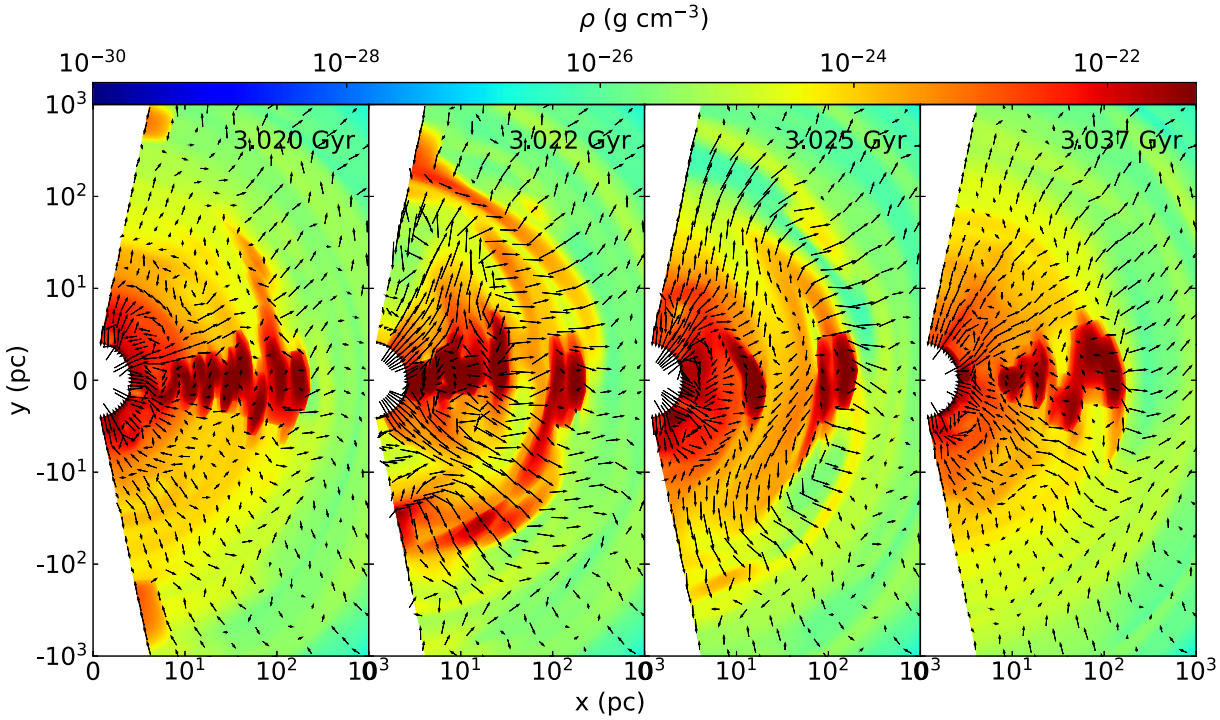

Figure 1. The time sequence of a density map for one cycle of an AGN burst for the fiducial model (k05). The arrows in each plot indicate the velocity vectors. From the left, the density map corresponds to preburst (3.02 Gyr), ongoing-burst (3.022 Gyr), postburst (3.025 Gyr), and quiescent (3.037 Gyr) periods, respectively. The lengths of the velocity vectors are scaled logarithmically in order to show the stream clearly.

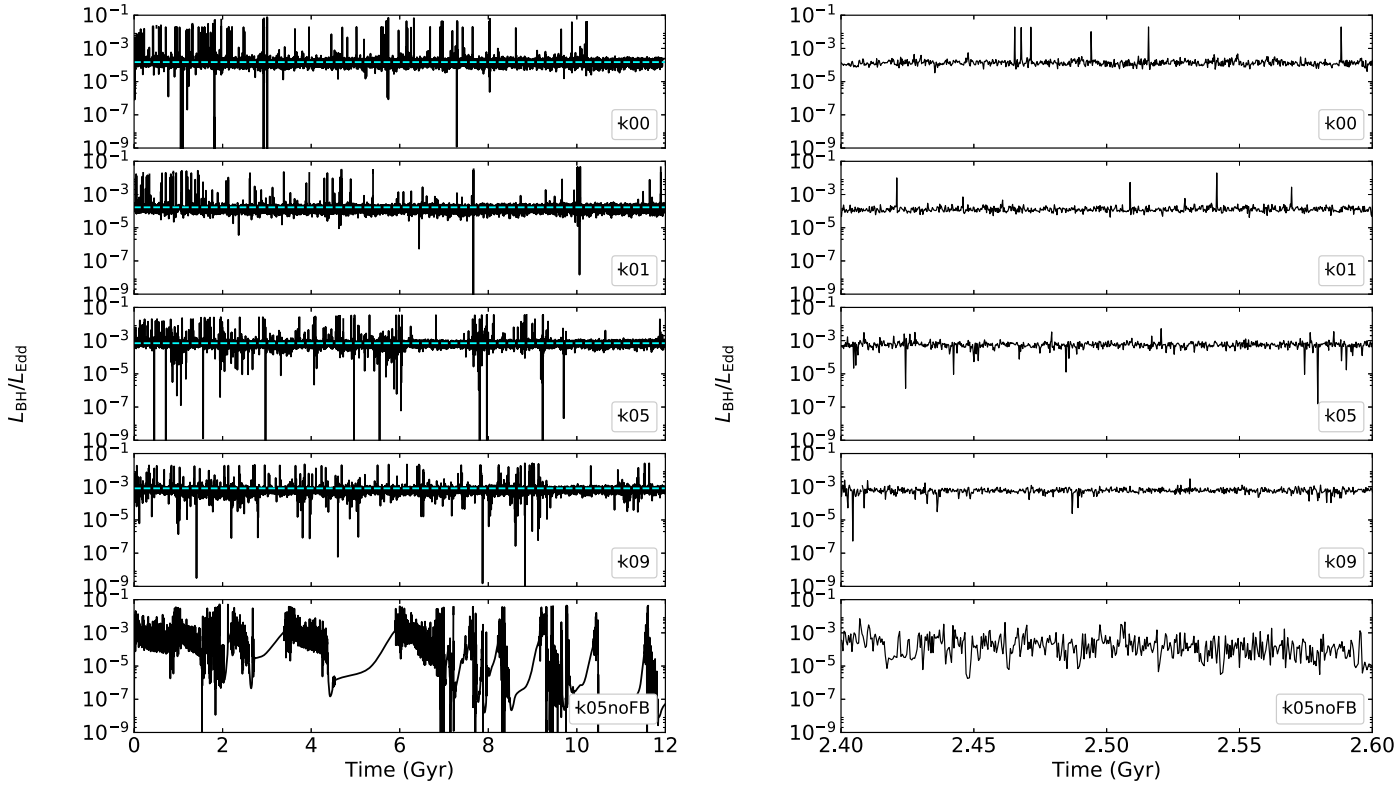

Figure 2. Light curves of AGN luminosity as a function of time for the models with different amounts of galactic rotation. The left panel shows the results over the entire evolution, and the right panel shows the results over a shorter time interval. In the left panel, the horizontal cyan line represents the median value of the light curves.

stronger radiation and winds, which more strongly expel the gas surrounding the black hole. This results in a longer period of time during which the accretion rate is very small.

In the right panel of Figure 2, we plot the AGN light curve over a shorter time interval in order to compare the shape of the curve lines in different models. As discussed, all models with

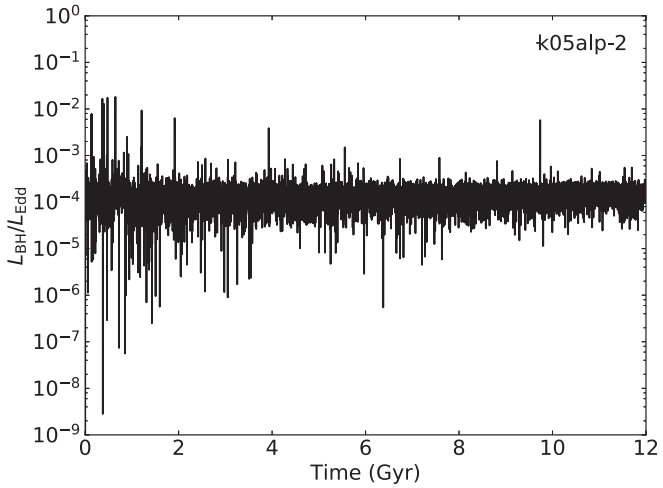

Figure 3. Light curve of AGN luminosity for the model with a low viscosity parameter, $\alpha_{visc} = 0.01$ (model k05alp-2).

AGN feedback have a similar shape, which is characterized by intermittent AGN bursts. The typical lifetime ($\sim 10^5$ years) of the AGN feedback is similar between the rotating models and the non-rotating model (see Paper I for a detailed discussion).

In the model without AGN feedback, k05noFB, the light curve variability does not imply AGN activity—it simply indicates the variation of corresponding mass accretion rate. While the mass accretion rate for the model without feedback in a non-rotating galaxy shows monotonic decrease (see noFB in Paper I), the rate in model k05noFB still fluctuates strongly. This is likely because, as in the case of black hole accretion flows, when the angular momentum of the gas is present, the motion of the gas is convectively unstable and such an instability produces turbulence and episodic accretion.

In the model k05noFB, The light curve shows intermittent breaks (e.g., from 4.3 to 6 Gyr). The explanation for this is as follows. The density in the midplane disk is very high. Without the influence of AGN feedback, which can heat and disturb the disk via wind and radiation, the formation of stars—and hence the stellar feedback by the supernova—is prone to be violent. Such violent stellar feedback can destroy the disk and expel large amounts of gas outward, which causes a strong decrease of the black hole accretion rate. If the galaxy rotates more slowly, the disk will shrink and thus the stellar feedback will be weaker. Therefore, these intermittent breaks take place only for the rapidly rotating galaxy without AGN feedback. However, we need to be mindful that, in our two-dimensional simulation, the stellar feedback on the disk could be overestimated. In the case of three-dimensional hydrodynamical simulations, the disk can fragment. Thus, the effects of the stellar feedback may not be strong enough to expel the gas and form a galactic fountain (Biernacki & Teyssier 2018). We will investigate this issue in a forthcoming study with a full three-dimensional simulation.

The BH accretion and the feedback are manipulated by the inflow of gas. For the rotating galaxy, such inflow is feasible only when the angular momentum of gas is transported outward. As a result, the value of the viscosity parameter is of particular importance. While the α_{visc} value remains uncertain, we set the α_{visc} value to 0.1 for most simulations. For comparison, we also carry out one run with $\alpha_{visc} = 0.01$ (k05alp-2) that is otherwise the same as the model k05. Figure 3 shows the AGN light curve for this model. Compared to the result shown in Figure 2, we can see that the mean

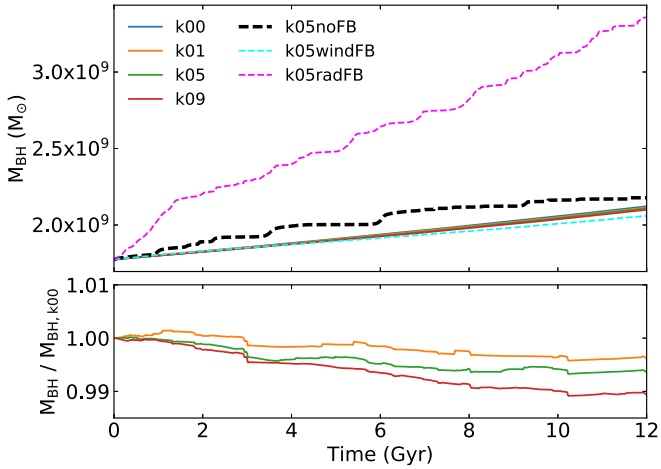

Figure 4. Mass evolution of BH for various models: solid lines represent each model with different galactic rotation. Black, cyan, and purple dashed lines indicate the BH mass growth for the model with no AGN feedback, purely mechanical feedback, and purely radiative feedback, respectively. In the bottom panel, the BH mass growth rates for k01, k05, and k09 are normalized by $M_{BH,k00}$.

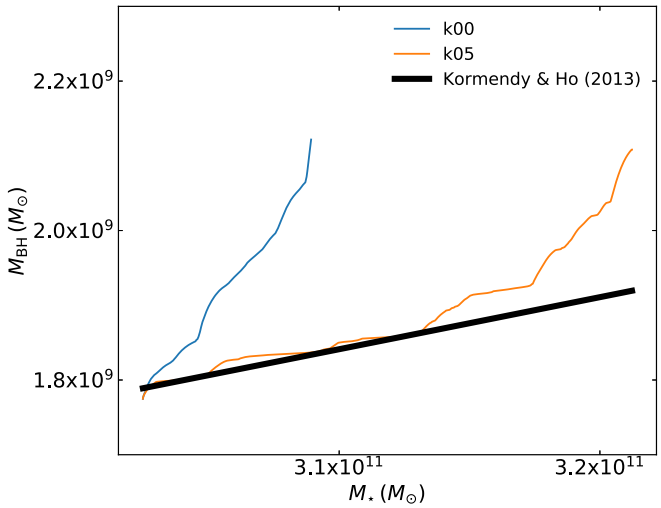

Figure 5. The relations between M_{BH} and $M_\star$. The blue and orange curves represent the results from the models k00 and k05, respectively. The thick black solid line represents the observed correlation of BH mass with bulge (elliptical) mass, which is derived with omission of pseudobulges (Kormendy & Ho 2013).

luminosity is significantly lower. This is because, when α_{visc} is smaller, the accretion timescale becomes longer, so the gas will stay in the disk for a longer time. Consequently, more gas will be consumed due to star formation, and thus the black hole accretion rate becomes smaller.

5.3. Mass Growth of the Black Hole

Mass accretion onto the BH is likely controlled by both AGN activity and galactic properties. As discussed in Paper I, the BH mass growth is regulated dominantly by mechanical feedback (i.e., AGN wind), which expels gas out of central region during the bursts. Unlike the AGN wind, irradiation by the AGN plays a complicated role. The radiative pressure drives gas outward, reducing the BH accretion. However, the radiative heating also suppresses star formation, preventing the gas from being depleted before it reaches the central BH, and

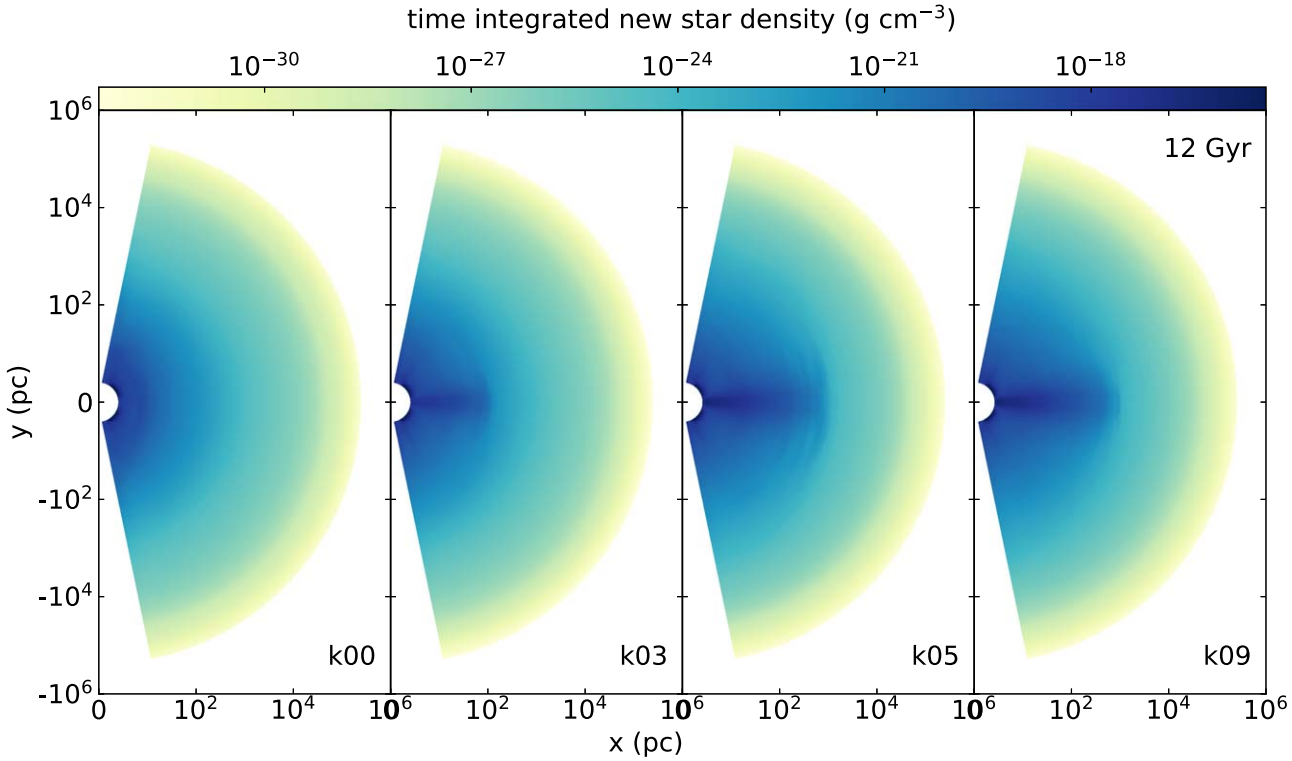

Figure 6. Time-integrated density of newly born stars at the end of the run for the models with different galactic rotation.

thus increasing the BH accretion simultaneously. The numerical results show that the latter effect is dominant, and hence the radiative feedback, in general, increases the BH growth rates. In Figure 4, the final BH mass in the model with pure radiative feedback (k05radFB, shown by the magenta dashed line) is two times larger than that in the rest of models, implying that pure radiative feedback is not effective in controlling the growth of the black hole mass. On the contrary, mechanical feedback plays the dominant role, as we see that the BH mass growth in the model k05windFB is similar to the full AGN feedback model (k05). This result was also found in the Choi et al. (2012) simulations, which had lower resolution but were 3D and included cosmological effects. In our work, we found that such primary roles for mechanical feedback and radiative feedback in regulating the BH mass growth are similar for the rotating and non-rotating galaxy models.

For the full feedback models, the difference in BH mass growth between the different galactic rotation models may not be significant, but we found a monotonic change with the rotation speed. The bottom panel of Figure 4 shows the relative growth rate between the rotating galaxies (k01, k05, k09) and the non-rotating galaxy (k00). It is clear that the BH accretion becomes more suppressed as a galaxy rotates faster. This can be attributed to the angular momentum, which prevents the gas from flowing inward.

It is believed that both the BH mass and the stellar mass may increase dramatically, mainly through galactic mergers at high-redshift epochs (e.g., Mihos & Hernquist 1996; Di Matteo et al. 2005; Cortijo-Ferrero et al. 2017; Goulding et al. 2018). However, the mergers are unlikely to dominate BH growth and the $M_{\rm BH} - M_{\star}$ relation has weak redshift evolution since $z \approx 2$ (Kocevski et al. 2012; Fan et al. 2014; Yang et al. 2018). Thus far, the previous numerical studies for AGN feedback in an early-type galaxy have a critical drawback: in most of the results, the BH growth over the galactic evolution is considerably larger than what is expected by the observed relation (Kormendy & Ho 2013). For example, in Gan et al. (2014), the final BH mass of models with AGN feedback is $M_{\rm BH,final}$ 10^9–10^{10} $M_{\odot}$, which is $5 \sim 30$ times larger than the initial mass, while the stellar mass increases by only several percent of the initial mass. In Figure 5, we show the $M_{\rm BH}$–$M_{\star}$ relation from our numerical data and the fitted formula from observation (Kormendy & Ho 2013). In our updated model, we found that the AGN feedback is effective in suppressing the BH growth and the result is consistent with the expected relationship: in previous work, the ratio of BH mass growth, $\Delta\ M_{\rm BH}/M_{\rm BH,init}$, is an order of magnitude larger than in the current result (e.g., Gan et al. 2014; Ciotti et al. 2017). In addition, we note that, when the host galaxy rotates faster, the black hole mass growth is more suppressed as a consequence of more active star formation in the mid plane disk, consuming more fuel before it accretes. (see Section 5.4 for more detailed discussion of the correlation between the angular momentum of the accreting gas and the star formation). We argue that the scatters shown in the observed correlation between the black hole mass and the stellar mass in the host galaxy may be ascribed to the degree of the galactic rotation. This also may provide clues for the long-standing questions of why and how BHs are no longer able to grow above the critical value, $M_{\rm BH,max} \sim 10^{11}\,M_{\odot}$, although these questions remain inconclusive (e.g., King 2016). In order to shed light on this problem, larger parameter studies (e.g., various initial gas density) are required. We will discuss this issue further in future work.

5.4. Star Formation

Figure 6 shows the newly born stars' density, which is time-integrated up to the end of runs. In a non-rotating galaxy (k00),

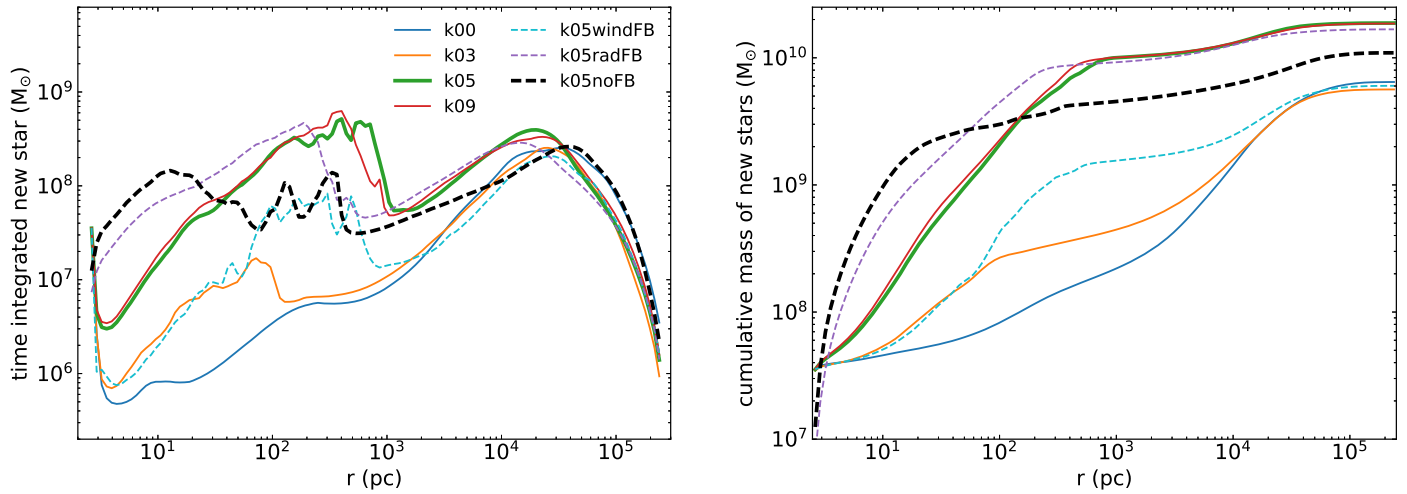

Figure 7. Left panel: θ-integrated mass of the newly born stars within each grid bin at a given radius at the end of the run. Right panel: enclosed mass of the newly born stars within a given radius at the end of the run. The two panels share the same denotation of lines.

stars form massively when the cold shells and filaments fall back onto the central region, resulting in quite spherically symmetric and centrally concentrated distribution (leftmost column). However, as we can see in the right three columns, if the host galaxy rotates, stars form dominantly at the cold midplane disk, whose size increases with the rotation speed. The midplane disk spreads up to 0.1, 0.3, 0.5 kpc for models k03, k05, k09, respectively.

Figure 7 shows the time-integrated mass of newly born stars as a function of radius. The left panel shows the θ-integrated total mass of new stars within each given radial bins. Note that, in our grid configuration, the bin size increases with the radius (see Section 4). We can see that, for rotating galaxies, there are two peaks for each curve. The outer peaks are purely due to the geometry effect, as explained in our Paper I. The inner peaks are absent in the case of the non-rotating galaxy and appear due to the rotation of the galaxy. From model k03 to k05, with the increase of the galaxy rotation, the amplitude of the peaks increases and the corresponding radius of the peaks becomes larger: the peak value of model k05 (the mild rotator) is an order of magnitude larger than that of model k03 (the slow rotator). To understand these results, we note that the peak location corresponds to the edge of the midplane disk shown in Figure 6. The overall star formation density in the disk is very high because star formation is strong there. This explains the presence of the peaks and why the location of the peak of the model k03 is smaller. However, interestingly, both the magnitude and location of the peaks "saturate" from model k05 to k09.

For the model without AGN feedback, k05noFB, the star formation occurs actively within 10 pc. We can see from the left panel of Figure 6 that the total mass of the new stars in this model is up to two orders of magnitudes larger than in the models with AGN feedback. This is because the surface density of the disk is high due to the lack of disturbance by wind and radiation from the AGN. If the entire disk were stable over the evolution time, the total mass of the new stars in k05noFB would be larger than that in the other models. However, as discussed, violent stellar feedback occurs intermittently, which expels large amounts of gas, reducing the total mass of new stars at $r > 10$ pc.

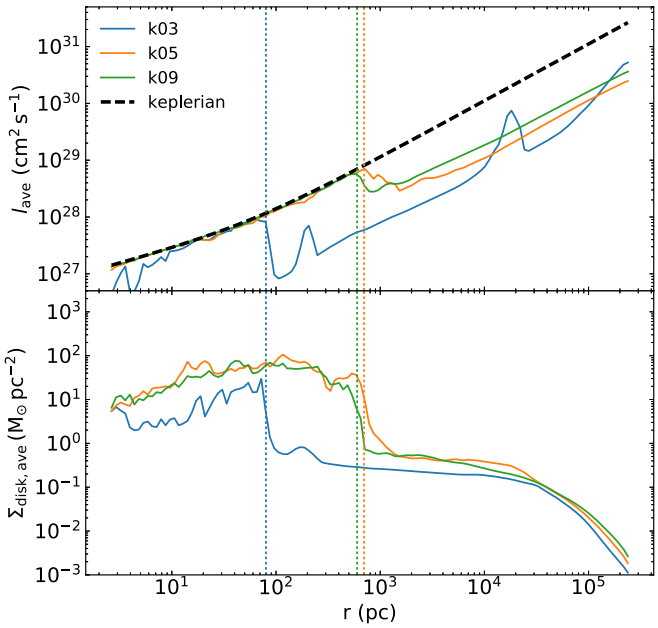

Figure 8. The time-averaged specific angular momentum (l_{ave}; upper panel) and surface density ($\Sigma_{disk,ave}$; lower panel) of the midplane disk as a function of radius. The integrated time is from 2 to 3 Gyr. The specific angular momentum is density-weighted, and the disk is identified within $\sim$15° above/below the equator. The black dashed line represents the Keplerian value with the given gravitational potential due to the black hole and dark matter. The vertical dotted lines mark the cutoff locations where the values drop sharply.

The right panel of Figure 7 shows the enclosed mass of the newly born stars within a given radius at the end of the run. It is clear that, as the galaxy rotates faster, the total mass of new stars becomes larger: the total masses of the newly born stars for the model k00 and k05 are $6.5 \times 10^9\,M_\odot$ and $1.9 \times 10^{10}\,M_\odot$, corresponding to 2% and 6% of the initial galactic stellar mass, respectively. This is because higher angular momentum leads the gas to stay longer at the midplane disk, inducing more active star formation.

The detailed disk properties are illustrated by the radial profiles of the specific angular momentum, l_{ave}, and the disk surface density, $\Sigma_{disk,ave}$. The results are shown in Figure 8. For the radial profiles, we average the data samples that lie in the time interval

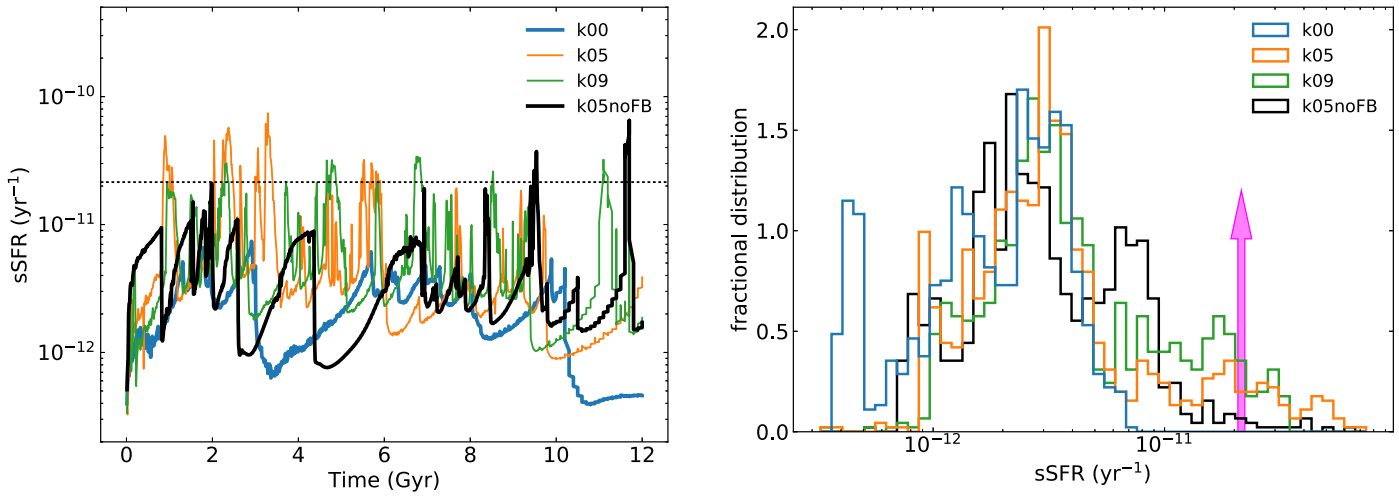

Figure 9. Left panel: the specific star formation rate as a function of time for the models with different galactic rotation. The horizontal dotted line in the left panel and the vertical arrow in the right panel represent the quiescence limit, below which the star formation is considered to be quenched (Franx et al. 2008). Right panel: the fractional distribution of the specific star formation rate. The colors of histogram, which represent each model, are the same as in the left panel.

between 2 and 3 Gyr. The disk surface density is computed within 15° above/below the equator (see the black dashed line in Figure 10). Once gas falls onto the midplane disk, that gas follows the Keplerian motion under the given gravitational potential. The size of the disk is initially determined by the angular momentum of the gas, but grows gradually due to the outward transport of angular momentum (Bu & Yuan 2014). For the slowly rotating model (k03), the sharp cutoff in the radial profiles occurs at a radius of 80 pc, which is an order of magnitude smaller than the fast rotators (k05 and k09). However, in our results, the disks of the galaxies that rotate faster than the k05 model are no longer stretched further, which produces saturation of the star-forming activity in the disk for models k05 and k09 (see Figure 7).

It is noteworthy that the disk surface density of model k03 is significantly lower than that of the fast rotators (k05 and k09). This is mainly because the midplane disk in the slowly rotating galaxy tends to be disrupted easily. We found that, over a large fraction of time, the midplane disk disappears in the k03 model, and thus the averaged value of the surface density for the integrated time interval becomes smaller. Such a short duration is ascribed to the AGN activity, which is more violent when the host galaxy rotates slower, as we discussed in Section 5.2. As a result, such relatively strong AGN feedback easily disrupts the disk, attenuating the star-forming activities in the disk, as seen in Figure 7.

Because the interplay between the AGN activity and star formation is complicated, the time evolution of the star formation rate should be examined in order to determine whether the AGN feedback induces or suppresses the star formation. The left panel of Figure 9 shows the specific star formation rate (sSFR) over the galactic evolution, which is computed via the star formation rate normalized by the stellar mass of the galaxy. As discussed in Paper I, the star formation rate is quite episodic as a consequence of the effects of AGN feedback. The horizontal dotted line is the quiescence limit (Franx et al. 2008), below which star formation is considered to be quenched. It is interesting to point out that, even for the model without AGN feedback, the star formation rate fluctuates significantly. Such fluctuation is not due to AGN feedback, but rather attributable to both the accretion process—which is intrinsically fluctuating—and the stellar feedback. Compared to the model with AGN feedback, the sSFR in the model without AGN feedback is relatively low. However, this does not imply that AGN feedback induces star formation: without AGN feedback, stellar feedback becomes intermittently violent and expels large amount of gas outward. In the right panel of Figure 9, the histogram shows that the typical value of the sSFR for all models is a few 10^{-12} years^{-1}.

Smethurst et al. (2018) showed observational evidence that, while the rapid quenching of star formation ($\tau \lesssim 1$ Gyr) is dominant for slowly rotating galaxies, the star formation in fast rotators remains active for a longer evolution time. They argued that it should be attributed to the different nature of the quenching mechanisms: the slowly rotating galaxies may be formed in major mergers, but the rapidly rotating galaxies are involved in multiple processes, such as secular evolution and minor mergers. However, Lagos et al. (2017) showed that the merged galaxies, which are slowly rotating due to the loss of angular momentum as a consequence of merging, still need to be quenched by feedback, otherwise the continuing gas inflow and star formation dominate over the negative effect of mergers. Our results show that AGN feedback effectively suppresses star formation activities in slowly rotating galaxies (see model k00 in Figure 9). In rapidly rotating galaxies, the negative effect of AGN feedback on star formation activity is relatively weak—this can be seen in models k05 and k09, where the histogram of the sSFR spreads out to high values.

In order to examine whether the inflowing gas ends up accreting onto the BH despite the depletion by massive star formation along its way, we compare the timescale between infall, $\tau_{\rm infall}$, and star formation, $\tau_{\rm SF}$:

$$\tau_{\rm infall} \equiv \frac{r}{v_r}, \tag{32}$$

$$\tau_{\rm SF} \equiv \max(\tau_{\rm cool}, \tau_{\rm dyn}), \tag{33}$$

where $\tau_{\rm cool}$ is the cooling timescale,

$$\tau_{\rm cool} \equiv \frac{e}{n^2\,\Lambda}, \tag{34}$$

where e is the internal energy of the gas, n is the number density, and Λ is the cooling rate, which is calculated from the most recent atomic database.[6] Here, $\tau_{\rm dyn}$ is the dynamical

[6] http://atomdb.org/

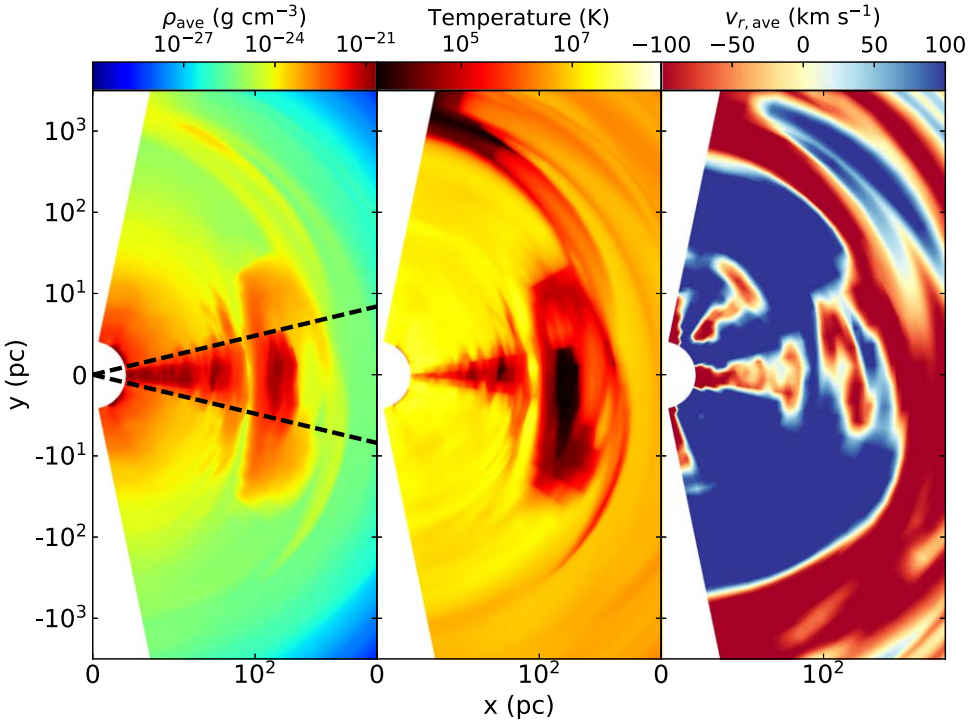

Figure 10. A contour map of the time-averaged density, temperature, and radial velocity. The midplane disk is within the black dashed line (leftmost panel), which is 15° above/below the equator.

timescale:

$$\tau_{\rm dyn} \equiv \min(\tau_{\rm Jeans}, \tau_{\rm rot}), \tag{35}$$

where $\tau_{\rm Jeans}$ and $\tau_{\rm rot}$ are the Jeans and rotational timescales, respectively:

$$\tau_{\rm Jeans} \equiv \left(\frac{3\,\pi}{32\,G\,\rho}\right)^{1/2}, \tag{36}$$

$$\tau_{\rm rot} \equiv \frac{2\pi r}{v_c}, \tag{37}$$

where v_c is the Keplerian velocity.

To examine different timescales, we need information concerning density, temperature, and radial velocity. These are calculated and shown in Figure 10. The results are from the data averaged for some periods, showing the midplane cold disk, along which the gas flows inward with a radial velocity of ~ -100s km s^{-1}. Using this averaged data set, we examine the timescale ratio between the infalls and the star formation, $\tau_{\rm infall}/\tau_{\rm SF}$, from Equations (32) and (33). The results for model k05 are shown in Figure 11. From this figure, we find that the infalling timescale is comparable to the star formation timescale over the entire disk in our fiducial model, k05. Consequently, in this model, a large fraction of infalling gas ends up accreting onto the black hole despite being depleted by star formation, triggering AGN activity as seen in Figure 2.

It should be noted that, in our simulation, star formation is computed by $\rho_{\rm SF} = \eta_{\rm SF}\rho/\tau_{\rm SF}$ without consideration of temperature and/or Jeans mass limiters. Here, $\eta_{\rm SF}$ is the star formation efficiency; we adopt a value of $\eta_{\rm SF} = 0.1$. The absence of the limiters may lead to an overestimate of star formation in high-temperature and low-density regions (e.g., the regions at large radii, $r \gtrsim 10s$ kpc). We checked that this does not affect our results significantly, but it will be taken into account in future work.

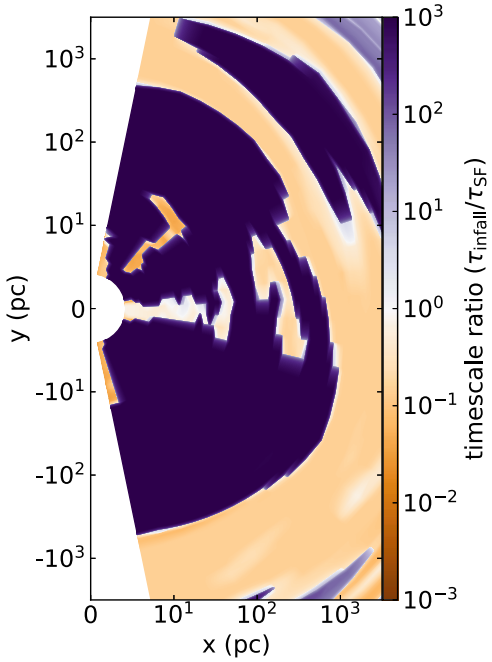

Figure 11. A contour map of the timescale ratio between the infalls and star formation, $\tau_{\rm infall}/\tau_{\rm SF}$.

5.5. AGN Duty Cycle

Following the procedure illustrated in Ciotti et al. (2017) for the low-rotation case, Figure 12 shows the percentage of the total simulation time spent above (right panel) and below (left panel) the given Eddington ratio. In the left panel, the vertical

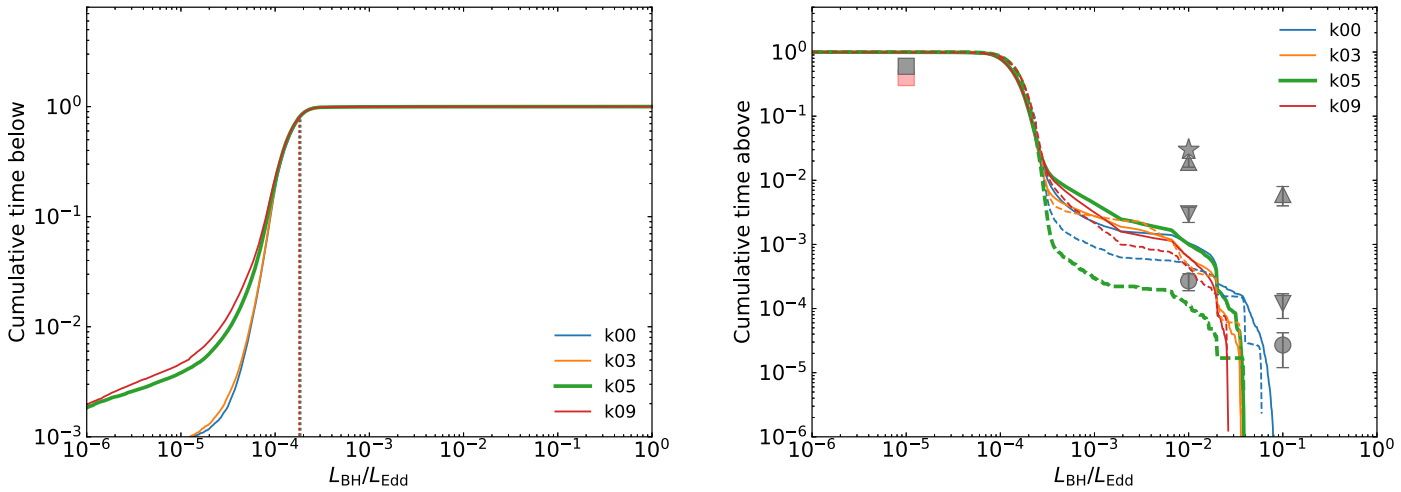

Figure 12. Percentage of total simulation time spent below (left panel) and above (right panel) the given Eddington ratios. In the left panel, vertical dotted lines indicate the Eddington ratio below which the AGN spends 80% of the total time. In the right panel, the solid and dashed lines represent fractional time computed for the entire time and the last 2 Gyr, respectively. The symbols represent observational data points. Square are from Ho (2009), circles from Greene & Ho (2007), upward-pointing triangles from Kauffmann & Heckman (2009), downward-pointing triangles from Heckman et al. (2004), and stars from Steidel et al. (2003).

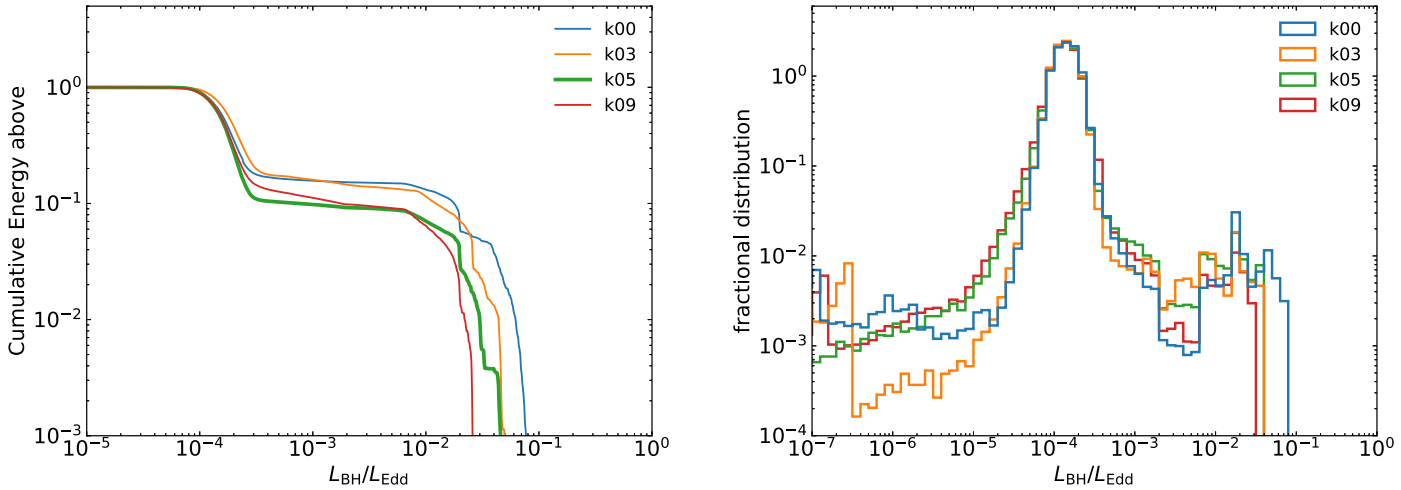

Figure 13. Left panel: percentage of the total energy emitted above the values of the Eddington ratios. Right panel: the fractional distribution of the black hole luminosity, which is normalized by the Eddington value. The colors of the histograms, which represent each model, are the same as in the left panel.

dotted lines indicate the Eddington ratio below which the AGN spends 80% of the total time. Every model spends most of the time at a low accretion regime (hot mode), which is consistent with the low detectability of active galaxies (e.g., Greene & Ho 2007).

In the right panel of Figure 12, the solid and dashed lines represent duty cycle profiles for the entire evolution time and the last 2 Gyr, respectively, during which the AGN spent time above the given Eddington ratio. The observational constraints are indicated by symbols: downward-pointing triangles are from Heckman et al. (2004), circles from Greene & Ho (2007), upward-pointing triangles from Kauffmann & Heckman (2009), and squares are from Ho (2009). Those data points are appropriate for comparing with the low-redshift results (i.e., dashed lines). The overall duty cycle is similar for all models, but we note that, as the galaxy rotates faster, the highest AGN luminosity that the AGN can reach gradually becomes smaller: the maximum AGN luminosity of the k09 model is $L_{BH,max} \approx 0.025\, L_{Edd}$, which is half of the maximum luminosity of the k00 model. The results show that all models lie below the observation data, but not by a large factor. In our numerical configuration, we assume that the gas is initially rarefied in the background medium, ignoring the presence of the gas that inflows from the intracluster medium or the gas that forms before 2 Gyr. Hence, we speculate that our numerical result for the AGN duty cycle in Figure 12 likely represents the case of lower limit.

Soltan (1982), Caplar et al. (2015), and Kollmeier et al. (2006) argued that, while AGNs spend most of their time in the low Eddington regime, they emit a significant fraction of energy in the high Eddington regime. The left panel of Figure 13 shows what percentage of the total energy is emitted above the given Eddington ratios. We found that, as the galaxy rotates faster, the fraction of emitted energy with a high Eddington ratio decreases. The total energy emitted in the cold mode (i.e., $L_{BH}/L_{Edd} > 0.02$) for model k09 is several percent of the entire energy emitted via AGN feedback, which is an order of magnitude smaller than that in the model k00. This trend also can be seen in the fractional distribution of the Eddington ratios (the right panel of Figure 13). It is clear that

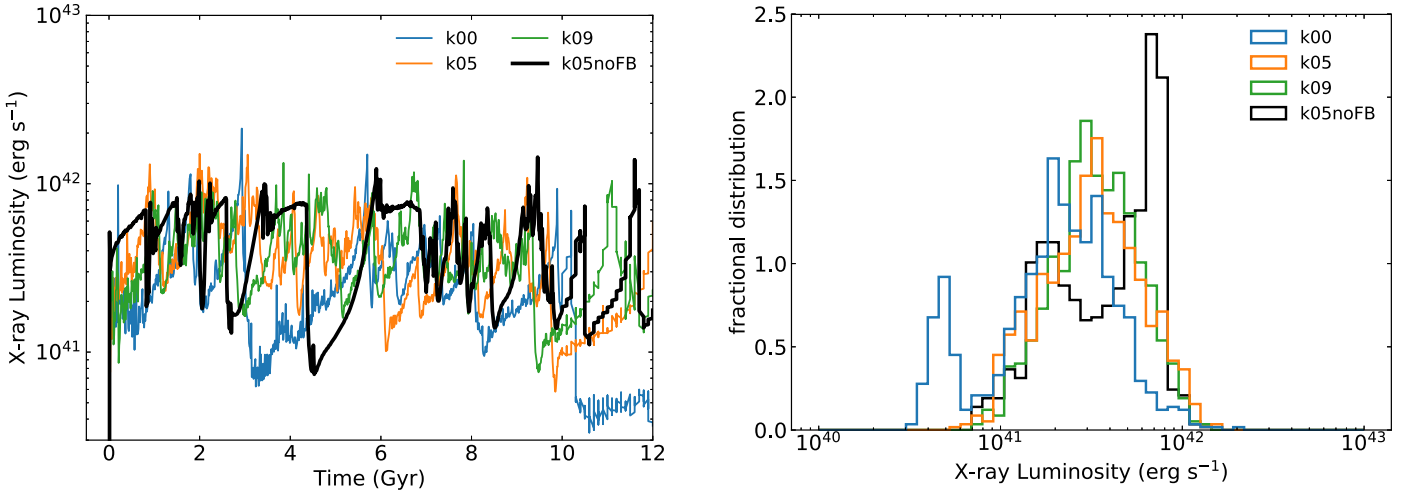

Figure 14. Left panel: X-ray luminosity in the 0.3–8 keV band over time for the different models. Right panel: the fractional distribution of X-ray luminosity. The colors of histogram, which represent each model, are the same as in the left panel.

angular momentum plays a role in reducing the strength of AGN feedback and that all our models emit less energy at high Eddington ratios than do real observed massive black holes.

5.6. X-Ray Properties of the Gas

We compute X-ray luminosity within an energy band range of 0.3–8 keV (the *Chandra sensitive band*).

$$L_{\rm X} = 4\,\pi \int_0^\infty \varepsilon(r)\, r^2\, dr, \tag{38}$$

where the emissivity is computed by $\varepsilon(r) = n_e(r) n_{\rm H}(r) \Lambda[T(r)]$, n_e and $n_{\rm H}$ are the number densities of electrons and hydrogen atoms, and $\Lambda(T)$ is the cooling function. We make use of the spectral fitting package, with the collisional ionization equilibrium XSPEC[7] (spectral model APEC) being used to calculate the cooling function (Smith et al. 2001).

The X-ray output is mostly emitted from the hot gas in the central region, where the effects of AGN feedback are likely dominant. The left panel of Figure 14 shows X-ray luminosity, $L_{\rm X}$, as a function of evolution time. We found that, for all models with AGN feedback, $L_{\rm X}$ strongly oscillates due to AGN activity, and it lies in the range $L_{\rm X} \sim 10^{41}$–10^{42} erg s^{-1} in general. For most of models, the dominant X-ray luminosity band is $\sim 3 \times 10^{41}$ erg s^{-1} (see the right panel of Figure 14). As discussed in Paper I, such values are consistent with observations (see also Pellegrini et al. 2018).

6. Summary and Conclusions

In this work, we have investigated the interplay between the AGN outputs released from the small-scale BH accretion and its host galaxy on a large scale. The primary goal is to understand the role of the angular momentum of accreting gas in such interplay. We performed two-dimensional hydrodynamic simulations, covering spatial ranges from several pc to ~100s of kpc. The galaxy model (including stellar distribution and dark matter) and physical processes (e.g., star formation, Type Ia and Type II supernovae) are described in Paper I. We adopt the most up-to-date "sub-grid" AGN physics as described in detail in Paper I, in which there are two modes of black hole accretion according to the mass accretion rate (i.e., hot and cold), and the description of wind and radiation are different in the two modes.

The high angular momentum is a natural barrier for BH accretion, due to angular momentum conservation. Most previous numerical studies of AGN feedback have assumed a galaxy model with a very low level of angular momentum. However, such a restriction is not a good approximation for most galaxies, even for early-type galaxies. In this work, we remove that restriction and investigate carefully how the level of angular momentum affects the interplay between an AGN and its host galaxy. In order to transport angular momentum, we adopt the α-viscosity model with an anomalous stress tensor. The fiducial value of the viscosity parameter is set to $\alpha_{\rm visc} = 0.1$ for most models in this work.

Our main findings are described below:

1. The general evolution picture of the AGN cycle in a rotating galaxy is qualitatively similar to that in a non-rotating galaxy. However, the details are significantly different. An important new feature is the presence of the midplane disk for the rotating galaxy, due to the angular momentum. As a result, gas fueling mainly occurs through the midplane, unlike to the case of non-rotating galaxy, in which the gas fuels the black hole in a random direction.
2. We found that, as the galaxy rotates slower, the AGN bursts occur more frequently at early evolution times, and the peak of the AGN light curve tends to be higher. The angular momentum of the gas plays a role in reducing the AGN activity in two ways: first, the mass accretion rate is reduced due to the presence of angular momentum. Second, it forms a midplane disk, within which a large fraction of gas is consumed via star formation before the gas reaches the BH.
3. The reduced AGN activity in the case of a rapidly rotating galaxy tends to disturb the midplane disk less strongly than in a slowly rotating galaxy. Consequently, as the host galaxy rotates faster, stars form dominantly at the midplane disk, and the total mass of new stars increases.
4. The overall profile of duty cycle is similar for all models with different levels of angular momentum, and it is

[7] http://heasarc.gsfc.nasa.gov/docs/xanadu/xspec/

somewhat below the observed data. Because we assume that the initial gas density is rarefied in the simulation, our results likely represent the minimum AGN activity in a given galactic environment. Too little energy is emitted at a high Eddington ratio compared to observations, which is likely also due to this assumption.

5. The X-ray luminosity is, in general, similar for all models, and the value is in a good agreement with the observed data.

D.Y. and F.Y. are supported in part by the National Key Research and Development Program of China (Grant No. 2016YFA0400704), the Natural Science Foundation of China (Grants 11573051, 11633006, 11650110427, 11661161012), the Key Research Program of Frontier Sciences of CAS (No. QYZDJSSW-SYS008), and the Astronomical Big Data Joint Research Center cofounded by the National Astronomical Observatories, the Chinese Academy of Sciences, and the Alibaba Cloud. Z.G. is supported by the Natural Science Foundation of Shanghai (Grant 18ZR1447200). This work made use of the High Performance Computing Resource in the Core Facility for Advanced Research Computing at Shanghai Astronomical Observatory.

ORCID iDs

Doosoo Yoon https://orcid.org/0000-0001-8694-8166
Feng Yuan https://orcid.org/0000-0003-3564-6437
Zhao-Ming Gan https://orcid.org/0000-0003-3886-0383
Jeremiah P. Ostriker https://orcid.org/0000-0002-6405-9904
Ya-Ping Li https://orcid.org/0000-0002-7329-9344
Luca Ciotti https://orcid.org/0000-0002-5708-5274

References

Anglés-Alcázar, D., Davé, R., Faucher-Giguère, C.-A., Özel, F., & Hopkins, P. F. 2017, MNRAS, 464, 2840
Auger, M. W., Treu, T., Bolton, A. S., et al. 2010, ApJ, 724, 511
Balbus, S. A., & Hawley, J. F. 1991, ApJ, 376, 214
Balbus, S. A., & Hawley, J. F. 1998, RvMP, 70, 1
Barnes, J. E., & Hernquist, L. 1996, ApJ, 471, 115
Barnes, J. E., & Hernquist, L. E. 1991, ApJL, 370, L65
Bertin, G., & Lodato, G. 2001, A&A, 370, 342
Biernacki, P., & Teyssier, R. 2018, MNRAS, 475, 5688
Bondi, H. 1952, MNRAS, 112, 195
Bournaud, F., Jog, C. J., & Combes, F. 2005, A&A, 437, 69
Bu, D.-F., & Yuan, F. 2014, MNRAS, 442, 917
Bu, D.-F., Yuan, F., Gan, Z.-M., & Yang, X.-H. 2016, ApJ, 823, 90
Caplar, N., Lilly, S. J., & Trakhtenbrot, B. 2015, ApJ, 811, 148
Choi, E., Ostriker, J. P., Naab, T., & Johansson, P. H. 2012, ApJ, 754, 125
Ciotti, L., Morganti, L., & de Zeeuw, P. T. 2009a, MNRAS, 393, 491
Ciotti, L., & Ostriker, J. P. 1997, ApJL, 487, L105
Ciotti, L., & Ostriker, J. P. 2001, ApJ, 551, 131
Ciotti, L., & Ostriker, J. P. 2007, ApJ, 665, 1038
Ciotti, L., & Ostriker, J. P. 2012, in Hot Interstellar Matter in Elliptical Galaxies, Astrophysics and Space Science Library, Vol. 378 (Berlin: Springer-Verlag), 83
Ciotti, L., Ostriker, J. P., & Proga, D. 2009b, ApJ, 699, 89
Ciotti, L., & Pellegrini, S. 2017, ApJ, 848, 29
Ciotti, L., Pellegrini, S., Negri, A., & Ostriker, J. P. 2017, ApJ, 835, 15
Cortijo-Ferrero, C., González Delgado, R. M., Pérez, E., et al. 2017, MNRAS, 467, 3898
Czoske, O., Barnabè, M., Koopmans, L. V. E., Treu, T., & Bolton, A. S. 2008, MNRAS, 384, 987
Di Matteo, T., Springel, V., & Hernquist, L. 2005, Natur, 433, 604
Dorodnitsyn, A., Kallman, T., & Proga, D. 2016, ApJ, 819, 115
Dye, S., Evans, N. W., Belokurov, V., Warren, S. J., & Hewett, P. 2008, MNRAS, 388, 384
Emsellem, E., Cappellari, M., Krajnović, D., et al. 2011, MNRAS, 414, 888
Fabian, A. C. 2012, ARA&A, 50, 455
Fan, L., Fang, G., Chen, Y., et al. 2014, ApJL, 784, L9
Franx, M., van Dokkum, P. G., Förster Schreiber, N. M., et al. 2008, ApJ, 688, 770
Gammie, C. F. 2001, ApJ, 553, 174
Gan, Z., Yuan, F., Ostriker, J. P., Ciotti, L., & Novak, G. S. 2014, ApJ, 789, 150
Gofford, J., Reeves, J. N., McLaughlin, D. E., et al. 2015, MNRAS, 451, 4169
Goulding, A. D., Greene, J. E., Bezanson, R., et al. 2018, PASJ, 70, S37
Greene, J. E., & Ho, L. C. 2007, ApJ, 667, 131
Hayes, J. C., Norman, M. L., Fiedler, R. A., et al. 2006, ApJS, 165, 188
Heckman, T. M., Kauffmann, G., Brinchmann, J., et al. 2004, ApJ, 613, 109
Hernquist, L. 1989, Natur, 340, 687
Hernquist, L., & Mihos, J. C. 1995, ApJ, 448, 41
Ho, L. C. 2009, ApJ, 699, 626
Hopkins, P. F., & Quataert, E. 2010, MNRAS, 407, 1529
Hopkins, P. F., & Quataert, E. 2011, MNRAS, 415, 1027
Jaffe, W. 1983, MNRAS, 202, 995
Kauffmann, G., & Heckman, T. M. 2009, MNRAS, 397, 135
King, A. 2016, MNRAS, 456, L109
Kocevski, D. D., Faber, S. M., Mozena, M., et al. 2012, ApJ, 744, 148
Kollmeier, J. A., Onken, C. A., Kochanek, C. S., et al. 2006, ApJ, 648, 128
Kormendy, J., & Ho, L. C. 2013, ARA&A, 51, 511
Korol, V., Ciotti, L., & Pellegrini, S. 2016, MNRAS, 460, 1188
Krajnović, D., Alatalo, K., Blitz, L., et al. 2013, MNRAS, 432, 1768
Krajnović, D., Emsellem, E., Cappellari, M., et al. 2011, MNRAS, 414, 2923
Lagos, C. d. P., Theuns, T., Stevens, A. R. H., et al. 2017, MNRAS, 464, 3850
Lodato, G., & Rice, W. K. M. 2004, MNRAS, 351, 630
Maraston, C. 2005, MNRAS, 362, 799
Mathews, W. G. 1989, AJ, 97, 42
Mihos, J. C., & Hernquist, L. 1996, ApJ, 464, 641
Negri, A., Pellegrini, S., & Ciotti, L. 2015, MNRAS, 451, 1212
Negri, A., Posacki, S., Pellegrini, S., & Ciotti, L. 2014, MNRAS, 445, 1351
Negri, A., & Volonteri, M. 2017, MNRAS, 467, 3475
Novak, G. S., Ostriker, J. P., & Ciotti, L. 2011, ApJ, 737, 26
Novak, G. S., Ostriker, J. P., & Ciotti, L. 2012, MNRAS, 427, 2734
Ostriker, J. P., Choi, E., Ciotti, L., Novak, G. S., & Proga, D. 2010, ApJ, 722, 642
Parriott, J. R., & Bregman, J. N. 2008, ApJ, 681, 1215
Pellegrini, S. 2012, in Hot Interstellar Matter in Elliptical Galaxies, Astrophysics and Space Science Library, Vol. 378 (Berlin: Springer-Verlag), 21
Pellegrini, S., Ciotti, L., Negri, A., & Ostriker, J. P. 2018, ApJ, 856, 115
Proga, D. 2003, ApJ, 585, 406
Salpeter, E. E. 1955, ApJ, 121, 161
Sazonov, S. Y., Ostriker, J. P., & Sunyaev, R. A. 2004, MNRAS, 347, 144
Schawinski, K., Treister, E., Urry, C. M., et al. 2011, ApJL, 727, L31
Serra, P., Oser, L., Krajnović, D., et al. 2014, MNRAS, 444, 3388
Shakura, N. I., & Sunyaev, R. A. 1973, A&A, 24, 337
Shin, M.-S., Ostriker, J. P., & Ciotti, L. 2010, ApJ, 711, 268
Smethurst, R. J., Masters, K. L., Lintott, C. J., et al. 2018, MNRAS, 473, 2679
Smith, R. K., Brickhouse, N. S., Liedahl, D. A., & Raymond, J. C. 2001, ApJL, 556, L91
Soltan, A. 1982, MNRAS, 200, 115
Sonnenfeld, A., Treu, T., Gavazzi, R., et al. 2013, ApJ, 777, 98
Steidel, C. C., Adelberger, K. L., Shapley, A. E., et al. 2003, ApJ, 592, 728
Stone, J. M., & Pringle, J. E. 2001, MNRAS, 322, 461
Stone, J. M., Pringle, J. E., & Begelman, M. C. 1999, MNRAS, 310, 1002
Tacchella, S., Carollo, C. M., Renzini, A., et al. 2015, Sci, 348, 314
Tang, S., & Wang, Q. D. 2005, ApJ, 628, 205
Toomre, A. 1964, ApJ, 139, 1217
Xie, F.-G., & Yuan, F. 2012, MNRAS, 427, 1580
Xie, F.-G., Yuan, F., & Ho, L. C. 2017, ApJ, 844, 42
Yang, G., Brandt, W. N., Vito, F., et al. 2018, MNRAS, 475, 118
Younger, J. D., Hopkins, P. F., Cox, T. J., & Hernquist, L. 2008, ApJ, 686, 815
Yu, Q., & Tremaine, S. 2002, MNRAS, 335, 965
Yuan, F., Bu, D., & Wu, M. 2012, ApJ, 761, 130
Yuan, F., Gan, Z., Narayan, R., et al. 2015, ApJ, 804, 101
Yuan, F., & Narayan, R. 2014, ARA&A, 52, 529
Yuan, F., Yoon, D., Li, Y.-P., et al. 2018, ApJ, 857, 121